Comparing electrocatalytic and thermocatalytic conversion of nitrate on platinum-ruthenium alloys

Journal:	*Catalysis Science & Technology*
Manuscript ID	CY-ART-06-2021-001075.R2
Article Type:	Paper
Date Submitted by the Author:	27-Sep-2021
Complete List of Authors:	Wang, Zixuan; University of Michigan, Ortiz, Evan; University of Michigan Goldsmith, Bryan; University of Michigan, Chemical Engineering Singh, Nirala; University of Michigan, Chemical Engineering

SCHOLARONE™
Manuscripts

ARTICLE

Comparing electrocatalytic and thermocatalytic conversion of nitrate on platinum-ruthenium alloys

Zixuan Wang[a,b], Evan M. Ortiz[a,b], Bryan R. Goldsmith [a,b*], Nirala Singh[a,b*]

Nitrate is a significant water pollutant resulting from anthropogenic nitrogen fixation and other industrial processes. Heterogeneous thermocatalytic and electrocatalytic processes to convert nitrate to nitrogen or ammonia are proposed to follow similar reaction mechanisms. However, there are no studies comparing these two processes on the same catalyst surface under similar reaction conditions. Here, we study both reactions on a series of Pt_xRu_y/C alloys to identify similarities and differences. For both reactions, we find that catalyst activity is correlated to both hydrogen and nitrate adsorption energies, signifying the importance of hydrogen and nitrate coverage in both systems. We measure that PtRu catalysts, recently reported to enhance electrocatalytic nitrate reduction, are also more active for thermocatalytic nitrate reduction than Pt. However, the effect of pH on reaction rates is considerably different between the two reactions, indicating that electrochemical-specific steps differentiate the two processes. We analyze the cost of converting nitrate to ammonia through both thermocatalytic and electrocatalytic reduction under different conditions on the same catalyst to compare which process is more cost-effective and capable of approaching the rates of commercial Haber-Bosch ammonia production.

Introduction

Modern agricultural processes release excess nitrate (NO_3^-),[1] polluting fresh water sources and posing a considerable threat to human[2,3] and ecological health.[4] Current physical nitrate removal techniques in use at water treatment plants include ion exchange and reverse osmosis. Although both options are efficient, they produce a concentrated nitrate waste stream that incurs a high financial cost for disposal.[5] Biological nitrate treatment can convert nitrate to nitrogen (N_2) or ammonia (NH_3); however, this process is slow, requires organic nutrients, and cannot treat streams with cellular toxins.[6] Thermocatalytic nitrate reduction (TNO$_3$RR) and electrocatalytic nitrate reduction (ENO$_3$RR) can address many of the concerns and limitations in current processes and promote the rapid conversion of nitrate to either N_2 or NH_3.[7–11] Many studies in this field have focused on closing the nitrogen cycle by exploring catalysts that are selective for N_2 production. However, recent works emphasize the high economic utility of recycling nitrate to value-added NH_3.[12–14] Producing NH_3 from nitrogen species in water could supply ~25% of NH_3 produced by the Haber-Bosch process, potentially offsetting ~1.5×10^6 TJ of energy consumption and ~60 Mt equivalent CO_2 emissions.[15,16] The market price of NH_4NO_3 from nitrate conversion was estimated

to be comparable to that from the Haber-Bosch process, assuming a low-cost, selective, and active catalyst exists.[9] However, most catalysts do not meet all of these criteria, making it difficult to implement TNO$_3$RR or ENO$_3$RR industrially.

There are no reports directly comparing the same catalysts under similar operating conditions for TNO$_3$RR and ENO$_3$RR to understand the similarities and differences between both reactions. It is essential to evaluate both systems to understand their capability to remediate nitrate while generating ammonia. Renewable electricity can either indirectly provide H_2 from water splitting that dissolve into an aqueous solution to convert nitrate over a catalyst in TNO$_3$RR or directly drive ENO$_3$RR by electrochemically reducing nitrate with protons over an electrocatalyst (**Scheme 1**). Most studies of TNO$_3$RR have used Pd-based catalysts that are effective for converting nitrite to N_2.[17–20] However, Pd is an expensive platinum group metal and requires a promoter metal to initiate nitrate reduction to nitrite. Non-precious metals have been explored for TNO$_3$RR to reduce catalyst costs, but are selective towards undesirable products such as nitrite, NO, or N_2O.[10,21] Additionally, TNO$_3$RR requires materials that can dissociate H_2. In contrast to TNO$_3$RR, the ENO$_3$RR can use materials that are less active toward H_2 dissociation by tuning the applied potential. In both TNO$_3$RR and ENO$_3$RR, there is no consensus for the best catalyst for nitrate conversion to ammonia.

[a.] Department of Chemical Engineering, University of Michigan, Ann Arbor, Michigan 48109-2136, USA
[b.] Catalysis Science and Technology Institute, University of Michigan, Ann Arbor, Michigan 48109-2136, USA
*Corresponding author(s)
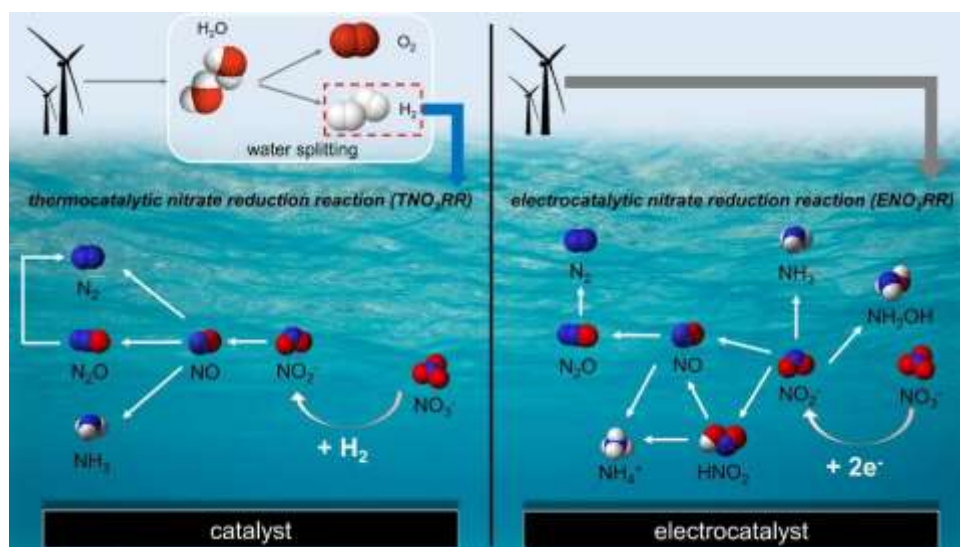
Scheme 1 Simplified reaction mechanism for thermocatalytic nitrate reduction reaction (TNO$_3$RR)[10] and electrocatalytic nitrate reduction reaction (ENO$_3$RR).[22] The major products and intermediates are shown for each reaction. The proposed rate-determining step is the reduction of nitrate to nitrite for both reactions. Renewable electricity can provide H$_2$ gas from water splitting in TNO$_3$RR or directly drive ENO$_3$RR. Color legend: O atom = red; N atom = blue; H atom = white. Oxidation reactions at the ENO$_3$RR counter electrode are not included.

Studying catalysts for TNO$_3$RR and ENO$_3$RR on a comparable basis would identify critical mechanistic similarities and differences. **Scheme 1** gives a comparative overview of the simplified reaction mechanisms for TNO$_3$RR[10] and ENO$_3$RR.[22] The rate-determining step (RDS) for both TNO$_3$RR and ENO$_3$RR is often the reduction of nitrate to nitrite.[10,23–27] Additionally, under judicious control of the operating conditions and catalyst, both reactions produce N$_2$ and NH$_3$ as the major products and nitrogen oxide compounds as less abundant products. However, the effects of the driving chemical potential for reduction (H$_2$ for TNO$_3$RR and applied potential for ENO$_3$RR), pH, nitrate concentration, and catalyst on both reactions have not been compared. Comparing thermocatalytic and electrocatalytic reactions has been valuable to improve the understanding of bio-oil hydrogenation,[28–30] H$_2$O$_2$ production,[31] and CO$_2$ reduction,[32] and can provide further insight into nitrate reduction.

We recently used density functional theory (DFT) and microkinetic modeling to generate theoretical activity volcano plots as a function of the N and O atomic adsorption energies as descriptors for the ENO$_3$RR activity.[25] The N and O adsorption energies are descriptors of activity because they scale with the adsorption strengths of nitrate reduction intermediates and associated activation barriers through adsorbate scaling and Brønsted-Evans-Polanyi relationships. Using these volcano plots, we identified Pt$_3$Ru as a promising electrocatalyst and experimentally validated this prediction for ENO$_3$RR on a series of Pt$_x$Ru$_y$/C alloys. Results showed that Pt$_{78}$Ru$_{22}$/C was greater than 10 times more active than Pt/C at pH = 0 and 0.05 V vs. RHE.[33] The kinetic enhancement resulted from Pt$_{78}$Ru$_{22}$ having high nitrate and hydrogen coverage on the surface. We hypothesize that if the catalytic mechanisms and RDS on Pt$_x$Ru$_y$/C alloys for ENO$_3$RR and TNO$_3$RR are similar, then a similar rate enhancement should be observed for TNO$_3$RR.

In this work, we study Pt/C, PtRu/C, and Pt$_{75}$Ru$_{25}$/C for TNO$_3$RR and ENO$_3$RR under various operating conditions (i.e., pH, hydrogen partial pressure, nitrate concentration, applied potential) to compare thermocatalytic and electrocatalytic approaches for nitrate reduction. We find that increasing the hydrogen (electro)chemical potential (0.1 to 1 atm H$_2$ and 0.15 to 0.05 V vs. RHE) increases the rate of nitrate conversion and that the ranking of catalyst activity is the same for ENO$_3$RR and TNO$_3$RR, that is, Pt/C << PtRu/C < Pt$_{75}$Ru$_{25}$/C. This change in activity from increasing Ru content in the alloy is attributed to increasing the adsorption strength of nitrate, hydrogen, and intermediates. Similarly, increasing the nitrate concentration increases reaction rates in ENO$_3$RR and TNO$_3$RR for PtRu/C. However, at concentrations above 0.5 M NO$_3^-$, ENO$_3$RR activity decreases due to surface poisoning by nitrate. Unlike hydrogen driving force and nitrate concentration, which similarly affect catalyst activity, the effect of the pH and the apparent activation energies were different for ENO$_3$RR and TNO$_3$RR on the PtRu/C catalyst. This finding implies that pH has a more complex role in the nitrate reduction mechanism than previously developed microkinetic models based on Langmuir-Hinshelwood surface reactions might suggest, and that there are fundamental differences between the two reactions. Despite these differences, certain catalyst properties (such as stronger nitrate adsorption) or reaction conditions (more available adsorbed hydrogen) increase the TNO$_3$RR and ENO$_3$RR rates in a way that is qualitatively captured by the existing theoretical volcano plot.[25,33] We compare the TNO$_3$RR and ENO$_3$RR performance on PtRu/C to rates and operating costs for industrial ammonia synthesis to evaluate the feasibility of both systems. Our results show that TNO$_3$RR on PtRu/C at pH 1 produces NH$_3$ at comparable rates to the Haber-Bosch process and, depending on the regional cost of H$_2$, can have lower operational costs than the USDA standard cost per tonne of NH$_4$NO$_3$. Ultimately, this work clarifies mechanistic similarities

and differences between TNO_3RR and ENO_3RR and serves as a model for evaluating catalytic systems for industrial implementation of nitrate reduction technology.

Experimental Methods

Material Synthesis and Characterization

A $NaBH_4$ reduction synthesis was used to synthesize $Pt_{75}Ru_{25}/C$.[33] The carbon black (Vulcan XC 72; Fuel Cell Store) was pretreated at 400 °C for 2 hrs to remove surface impurities. Afterwards, the support was suspended and sonicated in Millipore water (18.2 MΩcm, Millipore MilliQ system) for 15 min. Measured concentrations of $RuCl_3$ (38% Ru; Alfa Aesar) and H_2PtCl_6 (38–40% Pt; Sigma Aldrich) in Millipore water were added to the solution and stirred for another 15 min before 40 mg of $NaBH_4$ (Sigma Aldrich) dissolved in 25 mL of Millipore water were added to accelerate the reaction. The final solution was stirred for 2 hrs before centrifuging three times at 3000 rpm for 8 min each and washed with Millipore water. The recovered solid was dried overnight in an oven at 80 °C in air. All commercial catalysts (Pt/C and PtRu/C) were purchased from Fuel Cell Store. For the nitrate concentration and pH effect studies, we used the commercial PtRu/C instead of the most active synthesized $Pt_{75}Ru_{25}/C$ because a single batch of commercial PtRu/C was sufficient to perform all studies. Using $Pt_{75}Ru_{25}/C$ for these studies would require multiple batch syntheses and introduce batch-to-batch variations in the measurements.

The final metal loadings were determined by using thermogravimetric analysis (TGA) on a Shimadzu TGA-50H in a quartz pan. All catalyst samples were pretreated under He at 100 °C for 30 min to remove surface contaminants and adsorbed water. Samples were heated to 700 °C at 10 °C/min in air to oxidize all the carbon.[34,35] The metal weight loading was determined by dividing the final weight by the initial weight prior to the temperature ramp. X-ray diffraction (XRD) analysis was conducted using a Rigaku Miniflex XRD with Cu Kα radiation and a Ni filter (λ = 1.5418 Å). The 2ϑ range (10° < 2ϑ < 90°) was scanned at 5°/min with a 0.02° step size. Crystallite sizes were estimated using the Scherrer equation and the Pt and Ru peaks were referenced to #04-0802 and #06-0663, respectively, from JADE XRD processing software. Imaging and chemical characterization of the catalysts were performed with scanning electron microscopy (Nova 200 Nanolab; Thermo Fisher) coupled with energy-dispersive X-ray spectroscopy (SEM/EDX).

Thermocatalytic Nitrate Reduction Experiments

Thermocatalytic nitrate reduction activity was measured in a 125 mL 3-neck jacketed flask (ChemGlass) at atmospheric pressure. For all experiments, 10 mg of catalyst was suspended in 100 mL of Millipore water and stirred at 500 rpm. The solution was sparged with H_2 (Cryogenic Gases) for at least 30 min to remove dissolved oxygen and reduce the catalyst. The H_2 partial pressure (0.1–1 atm) was adjusted accordingly by co-feeding Ar (Cryogenic Gases) while keeping the total flow rate consistent at 250 mL/min. The temperature (20–50 °C) of the reactor was controlled via a refrigerated/heated bath circulator (Fisher Scientific). Desired concentrations of nitrate (1–100 mM $NaNO_3$) were added to the reactor at the beginning of the reaction after H_2 pretreatment. For lower concentrations of nitrate (≤10 mM $NaNO_3$), a sample was collected every 3 min for the first 15 min. At higher nitrate concentrations (>10 mM $NaNO_3$), a sample was collected every 15 min to ensure accurate rate quantifications under differential conditions. In all cases, a 1 mL syringe was used to extract the sample from the reactor before centrifuging at 3000 rpm for 5 min to separate the aliquot solution and catalyst particles. Nitrate, nitrite, and ammonia concentrations were measured using a UV-Vis spectrometer (Thermo Fischer, Evolution 350). The activity is reported as a turnover frequency (TOF) in moles of aqueous products (e.g., ammonia, nitrite) per mole of surface metal per minute.

Electrocatalytic Reduction Experiments

A single-compartment, 3-electrode, glass electrochemical cell (Pine Research) was used for electrochemical measurements with a clean graphite rod (Alfa Aesar, Ultra "F" purity) as the counter electrode. A single junction reference electrode (Pine Research, in 4 M KCl) was used in solutions with pH less than or equal to 7, and a double-junction reference electrode (Pine Research, in 10% KNO_3) was used in pH 10. Both reference electrodes were calibrated at 1 atm of H_2 (Cryogenic Gases) in different pH solutions. The cell initially contained 100 mL of electrolyte solution (pH 0: 1 M sulfuric acid; pH 1: 0.1 M sulfuric acid; pH 3: 0.1 M sodium citrate + 0.1 M citric acid; pH 5: 0.2 M sodium acetate + 0.2 M acetic acid; pH 7: 0.2 M sodium phosphate + 0.1 M citric acid; pH 10: 0.1 M sodium carbonate + 0.1 M sodium bicarbonate; Sigma Aldrich) with all anions in the solution confirmed to not react at the operating potentials. The selected buffers are chosen from those that have previously been used to study pH effects for electrochemical reactions where anion adsorption was not reported to significantly impact the results.[36] Prior to electrochemical experiments, N_2 (Cryogenic Gases) was sparged through the solution with a stir bar for at least 45 min to remove traces of dissolved O_2. Cyclic voltammogram (CV) scans after sparging confirmed the absence of dissolved O_2 from the solution and stability of the working electrode.

The working electrode was prepared and tested as described previously.[33] Briefly, a catalyst ink was prepared with a Nafion binder and deposited onto a glassy carbon rotating disk insert (Pine Research) to result in a total loading of 9.6 μg of catalyst, including carbon. The prepared electrodes were cleaned by cycling 50 times between hydrogen evolution and oxidation potentials (from –0.1 to 1.2 V vs. RHE) at 100 mV s⁻¹. Both hydrogen underpotential deposition (H_{upd}) and copper underpotential deposition (Cu_{upd}) were used to accurately evaluate the electrochemically active surface area (ECSA) of the catalysts as described previously.[33] After an 85% compensation for internal solution resistance as measured by electrochemical impedance spectroscopy, H_{upd} was determined by cycling between the onset of HER to Pt oxidation (pH 0: 0.06–1.3, pH 1:

0.07–1.3, pH 3: 0.05–1.3, pH 5: 0.05–0.8, pH 7: 0.06–1.3, and pH 10: 0.04–1.3 V vs. RHE), at a scan rate of 100 mV s^{-1} until the cyclic voltammograms were stable. The background-corrected hydrogen desorption charge and the average charge density of Pt (210 μC cm^{-2}) were used to determine the ECSA.

All chronoamperometry measurements were taken after an 85% compensation for internal solution resistance as measured by electrochemical impedance spectroscopy. The rotating disk electrode (RDE) was held at a rotation rate of 2500 rpm to eliminate mass transfer limitations and minimize differences in the pH between the bulk solution and at the electrode surface. We chose the rotation rate of 2500 rpm as it was sufficiently high where the reaction rates did not change with further increase in rotation rate. During the measurements, the bulk pH of the solution did not vary by more than a pH of 0.1. Currents were measured at four different applied potentials (0.05, 0.075, 0.1, 0.15 V vs. RHE) and recorded as the average current in the final 20 s. A baseline current was recorded in the electrolyte solution at each applied potential without the presence of nitrate. For ENO$_3$RR experiments, 20 mL of dissolved sodium nitrate in electrolyte solution was added to reach the desired concentration (0.01, 0.03, 0.1, 0.5, 1 M NaNO$_3$) before measuring the current at each applied potential.

Apparent Activation Energy Measurements

For ENO$_3$RR measurements, reduction currents were recorded for 10 min at two applied potentials (0.05 V and 0.1 V vs. RHE) and four different temperatures (T = 10, 20, 25, 30 °C) after compensating for 85% of the internal solution resistance. The TNO$_3$RR experiments were prepared using similar methods as previously described and operated at four different temperatures (T = 20, 30, 40, 50 °C). A heating/cooling jacket was used with a refrigerated/heated bath circulator (Fischer Scientific) to maintain the desired temperature. The difference in the temperature ranges selected were due to limitations of the experimental setup. For ENO$_3$RR experiments above 30 °C, thermal expansion caused the glassy carbon electrode to pop out of the Teflon holder. A wider range of temperatures was used for thermocatalytic measurements to reduce the influence of experimental error on the results. The apparent activation energy (E_a) was evaluated from an Arrhenius plot of the current density or TOF.

Selectivity Measurements

ENO$_3$RR measurements from depositing catalysts onto glassy carbon did not generate high enough currents to allow for product quantification. Thus, 10 mg of powder Pt$_x$Ru$_y$/C catalysts were directly deposited on 2.5×2.5 cm^2 pieces of carbon felt (6.35 mm thick, 99.0%, Alfa Aesar) in 40 mL of 1 M H$_2$SO$_4$. To ensure all of the catalyst was deposited onto the carbon felt, the solution was mixed for 30 min with bubbling H$_2$ at 80 °C. In a two-compartment electrochemical cell separated by Nafion 117 membrane, these carbon felts (CFs) were attached to a graphite rod (AGKSP grade, ultra "F" purity, Alfa Aesar) for use as the working electrode for ENO$_3$RR selectivity experiments as previously described.[33]

Nitrate and select liquid-phase products (i.e., NO$_2^-$ and NH$_3$) were measured using UV-vis spectrometer (Thermo Fischer, Evolution 350). Nitrate was quantified using standard spectrometry techniques. 10 μL from the sample aliquot was acquired and diluted to 2 mL using Millipore water. 1 mL of this resulting, well-mixed solution was further diluted to 3 mL in a quartz cuvette (Fisher Scientific, Azzota Corp 10 mm). UV-Vis measurements were taken between 190–300 nm, and the nitrate concentrations were calculated via the adsorption peak at 220 nm.[37] Millipore water was used as the background and subtracted from the sample spectra, and a calibration curve was created using known concentrations of NaNO$_3$ in solution.

Nitrite (NO$_2^-$) was quantified via a modified Griess diazotization reaction.[37,38] 0.3 mL of the extracted sample aliquot was diluted to 1 mL and neutralized with 1 M NaOH. 40 μL of the Griess color reagent, which consisted of 2% sulfanilamide (Fischer Scientific, ≥98%) and 0.2% N-(1-napthyl)-ethylenediamine (Sigma Aldrich, ≥98%) in phosphoric acid (Acros Organics; 85%) diluted to 0.1 M, was added. The resulting solution was left in the dark for 30 min before measuring absorbances at 543 nm. Known concentration of calibration standards were made from NaNO$_2$ (>99.0%, Sigma Aldrich).

Ammonia was quantified by using the indophenol blue test[13,39] with 1 mL of the sample aliquot. 1 M NaOH (Sigma Aldrich, 99.99%) was added to the electrolyte solution to neutralize the acid to a pH of 12. This was followed by sequentially adding 122 μL of sodium salicylate (Sigma Aldrich, >99.5%), 27.3 μL of sodium nitroprusside dihydrate (Sigma Aldrich, >99%), and 40 μL of sodium hypochlorite solution (Sigma Aldrich, 4.00–4.99%) to the electrolyte solution and manually stirred together. The solution was covered and left for 40 min. The indophenol peak was identified as the maximum absorbance between 600–700 nm. A fresh 0.1 M HNO$_3$ electrolyte solution prepared with the indophenol blue method was used as the background and subtracted from the sample spectra. If the concentration of NH$_3$ was too high and oversaturated the detector, the solution was diluted and retested. A calibration curve was created using known concentrations of NH$_4$Cl (99.99%, Sigma Aldrich) and unknown NH$_3$ concentrations were calculated using the Beer-Lambert law.

The faradaic efficiency (FE) for ENO$_3$RR was calculated by dividing the charge required to form the total NH$_3$ measured by the total charge passed during the steady-state experiments. The total charge passed was calculated by integrating the reduction current over the duration of the experiment and the charge required from NH$_3$ was calculated by assuming that eight electrons are required to form one molecule of NH$_3$ from one molecule of nitrate.

Results and Discussion

Applied Potential vs. H$_2$ Partial Pressure on Pt$_x$Ru$_y$/C Performance for Nitrate Conversion

Here we study TNO$_3$RR and ENO$_3$RR on Pt/C, PtRu/C, and Pt$_{75}$Ru$_{25}$/C to compare the effect of hydrogen driving force. The
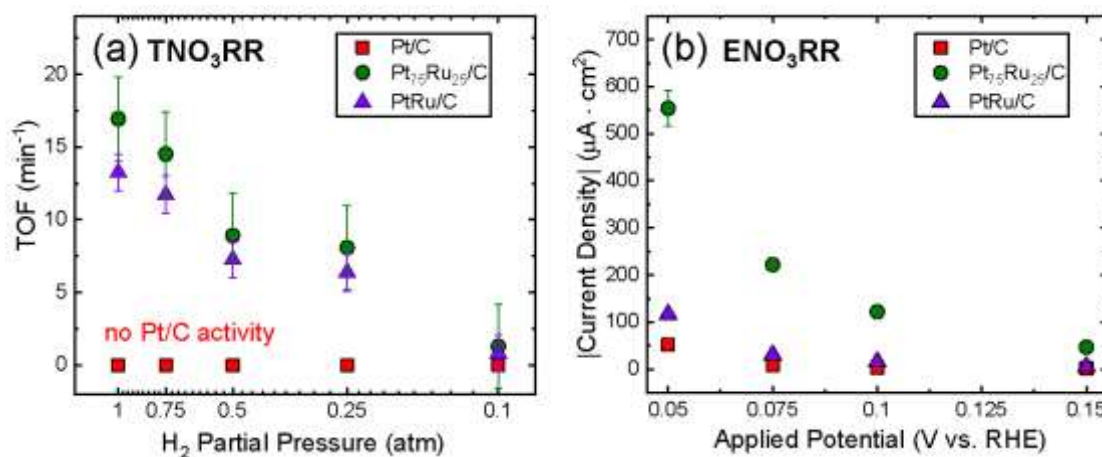
Fig. 1 Comparison of Pt_xRu_y/C activity for nitrate conversion at **(a)** different hydrogen partial pressures in thermocatalytic nitrate reduction reaction (TNO_3RR) based on ammonia production rate and **(b)** different applied potentials in electrocatalytic nitrate reduction reaction (ENO_3RR). All measurements were performed in pH 7 solution with 0.1 M $NaNO_3$. Assuming all electrons for ENO_3RR go to ammonia, a current density of 1 $mA·cm^{-2}$ is equivalent to a TOF of 31 min^{-1} on Pt/C. Thus, a current density of 100 $\mu A·cm^{-2}$ at 54% faradaic efficiency to ammonia corresponds to a TOF of 1.7 mol NH_3 per mol surface metal per minute. Note that we show hydrogen pressure increasing right to left in **Fig. 1a** to match the convention for less positive applied potential increasing the driving force for proton reduction in **Fig. 1b**.

weight loading of the catalysts was determined by TGA (**Fig. S1**), and corresponding crystallite sizes were calculated by applying the Scherrer equation to the XRD results (**Fig. S2**). The average nanoparticle sizes of Pt/C, PtRu/C and $Pt_{75}Ru_{25}$/C were 2.6, 2.4, and 3.7 nm, respectively (**Table S1**). SEM images of the Pt_xRu_y/C catalysts are provided in **Fig. S3**, and subsequent elemental analysis from EDX is shown in **Fig. S4**. No change in ammonia production rates is observed at rotation rates beyond 500 rpm (**Fig. S5**). As a result, a 500-rpm stir rate was used throughout TNO_3RR experiments to ensure no external mass transport limitations. Without the presence of metals on the Vulcan carbon support, no catalytic activity is recorded (**Fig. S6**). Additional details on material characterization and baseline measurements are provided in the Supporting Information.

We study the nitrate conversion TOF to NH_3 (for TNO_3RR) and total current density (for ENO_3RR) as a function of H_2 pressure and applied potential, respectively, for the Pt/C, PtRu/C, and $Pt_{75}Ru_{25}$/C materials in **Fig. 1**. These applied potentials and partial pressure ranges were chosen because (1) appreciable ENO_3RR activity is typically observed between 0.05 to 0.15 V vs. RHE and (2) typical TNO_3RR experiments are conducted with varying hydrogen partial pressures up to 1 atm. For all catalysts that showed activity, increasing the hydrogen driving force for reduction increases the rate of nitrate conversion. For TNO_3RR, the TOF on $Pt_{75}Ru_{25}$/C and PtRu/C increases as H_2 partial pressure increases. Likewise, the current density magnitudes from ENO_3RR for all Pt_xRu_y/C catalysts increase as the applied potential becomes more negative and approaches 0 V vs. RHE (the standard thermodynamic potential for 1 bar H_2). Because the H_2 partial pressure and potential are related via the Nernst equation, this finding implies that the driving force to form adsorbed hydrogen plays a similar and important role in both TNO_3RR and ENO_3RR. This qualitative relationship between partial pressure and potential is similar to that found for prior studies (e.g., phenol hydrogenation).[11,22,28,31,40–42] We also note that a change in

potential can bring different interactions between charged species and change the electronic energy of the metallic surface affecting both HER and ENO_3RR. However, this observation also supports the method of using the computational hydrogen electrode (where applied potential is equated to the chemical potential of hydrogen) to qualitatively model ENO_3RR.[25,33]

The activity of the catalysts follows the order $Pt_{75}Ru_{25}$/C > PtRu/C > Pt/C for both TNO_3RR (**Fig. 1a**) and ENO_3RR (**Fig. 1b**) at pH 7. These measurements demonstrate that the enhancement previously reported,[33] where PtRu/C and $Pt_{75}Ru_{25}$/C were more active than Pt for ENO_3RR at pH 0, also holds at pH 7. We previously attributed the higher ENO_3RR activity of Pt_xRu_y compared with pure Pt to increased adsorption strength of nitrate.[33] Pt_xRu_y alloys have ensembles of sites (e.g., Pt-Ru-Ru, Pt-Pt-Ru) that adsorb reactants and intermediates stronger than Pt. Our results here show similar activity trends hold for Pt_xRu_y/C towards TNO_3RR, suggesting that catalyst design metrics, such as the nitrate adsorption energy, are related for TNO_3RR and ENO_3RR under this set of conditions. The reason that PtRu/C is less active than $Pt_{75}Ru_{25}$/C, despite having more Ru and thus more sites with stronger adsorption, is rationalized by a theoretical volcano plot, where the nitrate adsorption is too strong and decreases the rate.[33] The decrease in activity for PtRu/C compared to $Pt_{75}Ru_{25}$/C is also observed for TNO_3RR, but to a lesser extent.

While the behavior of TNO_3RR and ENO_3RR with hydrogen pressure/applied potential and catalyst alloying are qualitatively the same, there are differences in the reactions when considering the quantitative activity of the catalysts. One difference in the behavior is that for Pt/C there was no measured activity during TNO_3RR, even with increasing the amount of catalyst in the reactor (**Fig. S6d**), whereas some catalytic activity was observed for ENO_3RR. More specifically, while Pt/C was entirely inactive for TNO_3RR compared to PtRu/C or $Pt_{75}Ru_{25}$/C (**Fig. 1a**), a current density of 52 μA cm^{-2} was recorded for Pt/C at 0.05 V vs. RHE during ENO_3RR (only 55%

lower than PtRu/C, **Fig. 1b**). Our results agree with previous studies that show no activity for Pt in TNO$_3$RR.[43] However, the Pt catalyst has been demonstrated to be active for the thermocatalytic hydrogenation of nitrite.[44] The inactivity of pure Pt relative to that of Pt$_x$Ru$_y$/C leads us to postulate that Ru is responsible for hydrogenation of nitrate to nitrite and both Ru and Pt sites participate in further hydrogenation of nitrite to ammonia. These results point to potential differences in the mechanism between electrocatalytic and thermocatalytic reduction on the surface of Pt and to differences in using H$_2$ pressure compared to electrochemical potential as the driving force for hydrogenation, namely the effect of potential on interactions with charge species such as nitrate and the charge of the electrode surface.

Nitrate Concentration on PtRu/C

The data in **Fig. 2** shows that both TNO$_3$RR and ENO$_3$RR have a positive rate order in nitrate on PtRu/C at low concentrations (<0.5 M NaNO$_3$) and a negative rate order in nitrate at higher concentrations (>0.5 M NaNO$_3$) for ENO$_3$RR. A positive rate order at low nitrate concentrations for TNO$_3$RR has been previously observed for kinetic studies on PdCu alloys.[45] For all applied potentials, ENO$_3$RR on PtRu/C follows the same qualitative trend and is the most active at 0.5 M NO$_3^-$ in pH 7 solution. The trends observed for ENO$_3$RR show the RDS is a surface reaction, which qualitatively agrees with a prior report that explores nitrate concentration effects on Pt.[46] A simple rate law for this reaction is:

$$rate = k\theta_H\theta_N \qquad (1)$$

where k is the rate constant of the surface reaction and θ_H and θ_N represent the hydrogen and nitrate coverages, respectively, and are controlled by their corresponding equilibrium adsorption constants and concentrations for those species (see SI for more details). At low nitrate concentrations, both θ_N and the current densities are directly proportional to the concentration of nitrate in solution. There is a decrease in reaction rate at high nitrate concentrations for ENO$_3$RR, suggesting that the nitrate is blocking surface sites for H$^+$ adsorption and inhibiting reduction. This hypothesis is supported by previous X-ray absorption near edge spectra measurements on Pt/C, where addition of nitrate to solution caused a decrease in hydrogen coverage, implying competitive adsorption between nitrate and hydrogen.[25] We were unable to accurately quantify TNO$_3$RR ammonia production rates using UV-Vis spectroscopy for nitrate concentrations greater than 0.1 M NO$_3^-$, so activities above that concentration are not included in **Fig. 2**. The ENO$_3$RR rates were measurable at these concentrations because the activity is based on the current density, rather than direct quantification of ammonia at short time scales. From previous experiments, we found selectivities for the alloys ranged from 93% to 98% at 0.1 V vs. RHE and pH = 1,[33] and assumed 100% selectivity to ammonia under these conditions. We note that at pH 7 at 0.1 V vs. RHE, the faradaic efficiency towards ammonia on PtRu/C is approximately 54%
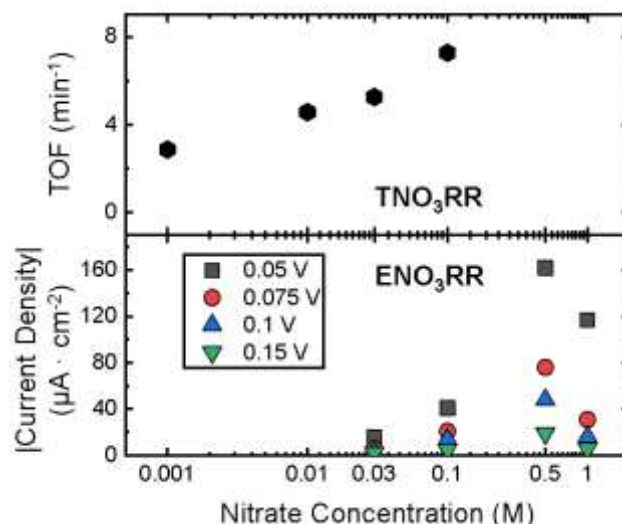

Fig. 2 The activity of PtRu/C as a function of nitrate concentration in pH 7 solution. The activity of the TNO$_3$RR and ENO$_3$RR is defined in TOF (min^{-1}) and |Current Density| (μA·cm^{-2}), respectively. All experiments were performed at room temperature (23.3 °C), and the hydrogen partial pressure for TNO$_3$RR was set at 0.5 atm.

(see below), thus the current density values shown in **Fig. 2** correspond to all nitrate reduction products, not specifically ammonia.

The ENO$_3$RR activity as a function of nitrate concentration is rationalized using the Langmuir-Hinshelwood model used to generate the rate law in Eq. 1 (**Fig. S7**). The fitted rate law captures that the activity for PtRu/C in pH 7 increases with nitrate concentration up to 0.4 M, but decreases at higher nitrate concentrations. For a surface reaction involving adsorbed hydrogen and adsorbed nitrate, increasing the nitrate concentration has a similar effect as increasing the nitrate adsorption strength, as both lead to higher nitrate coverages. The model provides a qualitative description of the relationship between ENO$_3$RR activity, nitrate adsorption energy, and nitrate concentration. Although, as discussed above, there is the possibility of a bifunctional (multi-site) mechanism on alloys, we do not see conclusive evidence that this is the case from our kinetic modeling and thus postulate only the simplest model that qualitatively describes the data. Further understanding the reaction chemistry and incorporating additional reaction steps would improve model fitting.

The results in **Fig. 1** and **Fig. 2** imply that the computational volcano plots[25,33] and a simple Langmuir-Hinshelwood model apply qualitatively to both TNO$_3$RR and ENO$_3$RR, where the rate is related to the amount of available hydrogen and the coverage of nitrate on the surface. This similarity may be due to the two reactions sharing a common RDS or catalyst properties that control their respective RDS. However, as observed for the contrast between activity for Pt/C in ENO$_3$RR and TNO$_3$RR, there are quantitative differences in TNO$_3$RR and ENO$_3$RR, which we explore in the following section.

pH Effects on Rate and Apparent Activation Energy of PtRu/C
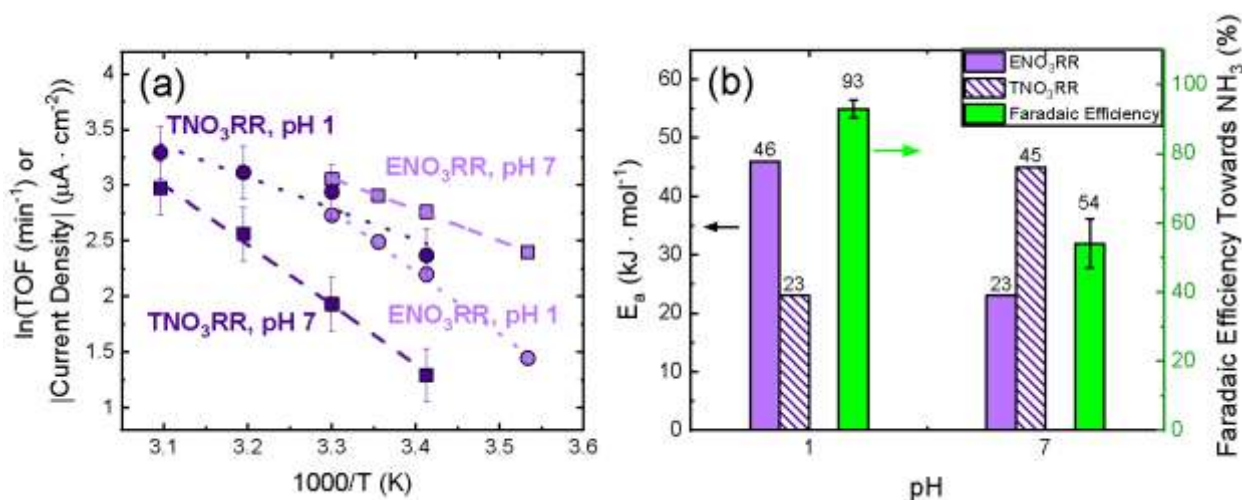
Fig. 3 (a) Arrhenius plots of PtRu/C for thermocatalytic nitrate reduction reaction (TNO$_3$RR) and electrocatalytic nitrate reduction reaction (ENO$_3$RR) at pH 1 and pH 7. Temperatures for TNO$_3$RR experiments range from 20–50 °C and 10–30 °C for ENO$_3$RR. The activity of the TNO$_3$RR and ENO$_3$RR is defined in TOF (min^{-1}) and |Current Density| (μA·cm^{-2}), respectively. **(b)** Comparison of apparent activation energy (E_a) and faradaic efficiency (FE) towards NH$_3$ across different solution pH and reaction systems. The light-purple solid bars denote E_a from ENO$_3$RR and dark-purple striped bars denote E_a from TNO$_3$RR. H$_2$ partial pressure was set at 0.5 atm and FE experiments were performed at 0.1 V vs. RHE.

Despite the similar effect of hydrogen chemical potential, alloying, and nitrate concentration between TNO$_3$RR and ENO$_3$RR, there are distinct differences when considering the effect of pH and apparent activation energies (E_a), **Fig. 3**. TNO$_3$RR shows higher activity at pH 1 than pH 7 (**Fig. 3a**). In contrast, the ENO$_3$RR rates are higher at pH 7 than pH 1. These rates are consistent with the order of the E_a for TNO$_3$RR and ENO$_3$RR, where the E_a for TNO$_3$RR is lower at pH 1 and the E_a for ENO$_3$RR is lower at pH 7 (**Fig. 3b**). The previously used volcano plots[25,33] and our Langmuir-Hinshelwood models do not incorporate the effect of pH (all calculations implicitly assume pH = 0). However, the large effect of pH and opposite trends for TNO$_3$RR and ENO$_3$RR reveal that a more complex mechanistic model than previously proposed is needed to understand this reaction. We will first discuss potential causes of the effect of pH on TNO$_3$RR and then discuss the influence on ENO$_3$RR in greater detail. Note that all measurements for ENO$_3$RR are at the same potential vs. RHE, so the thermodynamic effect of changing the pH has been considered, and the pH effects observed in **Fig. 3** are non-Nernstian.

We propose that the higher activity and lower E_a observed for TNO$_3$RR at lower pH is most likely because it is easier for nitrite to either decompose or hydrogenate to other products in acidic conditions.[47] At low pH, literature has indicated higher nitrite hydrogenation TOF rates through increased surface coverage of reaction intermediates, such as *NO and *HNO.[48] The E_a for TNO$_3$RR at pH 7 is 45 kJ mol^{-1}, similar to that of measurements of Pt group metals in neutral solution.[49,50] The lower E_a at pH 1 than pH 7 may arise from more favorable intermediate conversion to ammonia at low pH. It is also possible that the pH (and corresponding changes in the electrochemical double layer) affects the adsorption of nitrate, which would influence the rate.

The shift in activity and E_a for ENO$_3$RR with pH is more challenging to deconvolute than for TNO$_3$RR. This change in activity may either be due to a different RDS entirely at the different pH values or the same RDS, but with different coverages of the intermediates. Although the pH may affect nitrate adsorption energy and thus the reaction rate because the effect of pH is opposite for TNO$_3$RR than ENO$_3$RR, other pH effects likely play a role in the reaction. Similarly, the conversion of nitrite being faster at lower pH values (as described above for TNO$_3$RR) does not explain the trend in pH for ENO$_3$RR.

Previous reports hypothesize a mechanistic shift occurs with an increase in the pH of the electrolyte solution for ENO$_3$RR.[49,50] In acidic media, the concentration of H$^+$ correlates to the nitrate reduction activity.[49,50] As the pH increases, the reaction stops being dependent on H$^+$, and the hydrogen source is provided from H$_2$O. Similarly, in our results the FE for ENO$_3$RR changes from 93% at pH 1 to 54% at pH 7 (**Fig. 3b** and **Fig. S9**). Additional Tafel analysis provided limited insights on the mechanism due to the limited range of testing potentials (**Fig. S10**). However, previous literature indicate that this change is likely due to the reaction favoring an ammonia production mechanism at pH 1 and favoring a nitrogen production mechanism at more basic pH.[8] We note that gaseous products such as nitrogen are not measured in this study and future works to understand product distribution changes as a function of pH over a wide range of applied potentials are needed to understand the mechanism.

To investigate the role protons and water play in the ENO$_3$RR in more detail, the PtRu/C current densities for ENO$_3$RR for pH 0–10 at four different operating potentials vs. RHE are shown in **Fig. 4**. We also include the absolute current densities as a function of the potential vs. SHE in Fig. S11. The results in **Fig. 4** show that as the electrolyte pH increases, the ENO$_3$RR activity of PtRu/C increases from pH 0 to pH 3, with a plateau from pH 3 to pH 7, which may be due to effects from the reaction environment or changes in the catalyst due to pH. By examining the absolute current densities as a function of the potential vs. SHE, we observe similar trends that as the pH increases, the current densities for nitrate reduction increases (**Fig. S11**). At pH 10, where the current densities are the highest,

the catalyst may be forming Ru oxides above pH 9 that are artificially inflating the reduction currents.[51] It is also possible that the high activity results from favorable Ru lattice strains from subsurface oxide formation.[12] While XPS surface characterization of the catalyst before and after an extended 8-hour steady-state electrochemical experiment at 0.1 V vs. RHE and pH 10 shows marginally lower amounts of surface Ru, the low intensity of the spectra makes it difficult to deconvolute for Ru oxidation peaks (**Fig. S12**). A previous study of ENO₃RR on Rh and Pt reported that the reduction rate decreases with the concentration of hydronium ions decreasing from pH 0 to 4,[52] which is opposite to what we observe for PtRu/C. In that work, NaCl was added as the pH increased to maintain a constant ionic strength of the electrolyte. Because chloride is known to inhibit both Pt[53] and Rh[54,55] for ENO₃RR, the previously reported decrease in activity may be due to increasing chloride inhibition of catalyst sites, not the change in pH. It is possible that the ionic strength of the solution in our results is affecting the reduction currents and needs to be accounted for to obtain an accurate pH effect analysis. **Fig. S10** provides the ionic strength of the buffer solutions at each pH, ranging from 0.25 (pH 1) up to 2.5 M (pH 0). The ionic strengths vary from different pH solutions, but do not match the activity trends observed in **Fig. 4**, and so are not the sole cause of the pH effect.

The effect of pH on other electrocatalytic reactions has been studied extensively, and some of the findings for other reactions may be applied to ENO₃RR. Hydrogen binding energy is one proposed factor in which pH influences catalytic activity,[56,57] but other effects, such as the ionic strength of the buffer,[52,58] hydrogen equilibrium potential,[59] point of zero free charge (pzfc),[60–62] and water orientation and reorganization energy,[63–65] can also influence the activity. For hydrogen evolution, the activities for Pt group metals are much higher at lower pH values, but the reason is debated in several recent reviews and publications.[66–70] This enhancement is the opposite direction of what we observe for ENO₃RR. Oxygen reduction reaction (ORR) is more complicated, with ORR activity on Pt(111) increasing as the pH increases from 1 to 6 and decreasing with increasing pH past 11 and a predicted maximum at pH 9.[71] This trend is attributed to the ORR onset potential being positive and negative with respect to the pzfc of the electrode in acidic and basic solution, respectively, causing the switch in pH dependence. For ENO₃RR on PtRu/C, there seems to be a maximum with pH similar to ORR, but the ENO₃RR maximum occurs at pH 5 (excluding potential oxide effects at pH 10). Thus, one possible cause of the pH dependence of ENO₃RR could be differences in the surface charge of the electrode. From **Fig. S11** it is clear that although the voltage vs. RHE may be the same for ENO₃RR at two different pH values, the voltage vs. SHE is considerably different, which may play a significant role in the surface charge of the electrode. One possibility is that ENO₃RR increases with increasing pH from pH 0 to pH 3 when the potential is near 0 V vs. SHE, but at higher pH values where the electrode potential becomes more negative vs. SHE and the surface becomes overly charged, there is a maximum in activity from pH 3 to pH 7 because increasing the pH also causes the voltage vs. SHE to become too negative. Further experiments
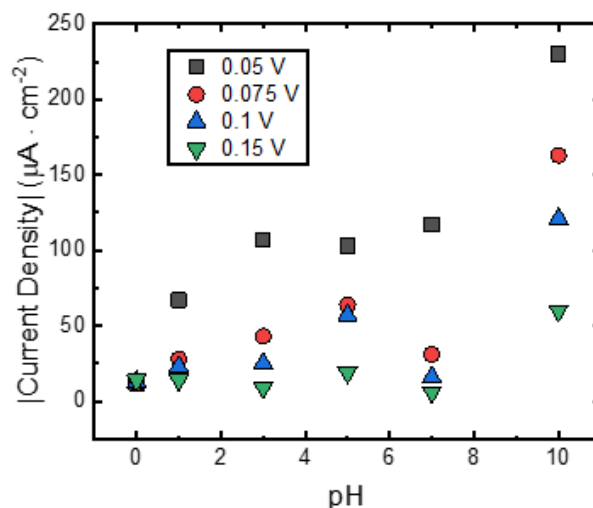

Fig. 4 Absolute current densities for pH 0–10 in 1 M NaNO₃ using PtRu/C at different applied potentials vs. RHE. The electrolyte solution at each pH is: pH 0 – 1 M H₂SO₄, pH 1 – 0.1 M H₂SO₄, pH 3 – 0.1 M sodium citrate + 0.1 M citric acid, pH 5 – 0.2 M sodium acetate + 0.2 M acetic acid, pH 7 – 0.2 M sodium phosphate + 0.1 M citric acid, pH 10 – 0.1 M sodium carbonate + 0.1 M sodium bicarbonate.

investigating the impact of the voltage vs. SHE on nitrate and water adsorption may explain some of the behavior with pH observed here.

Although a Langmuir-Hinshelwood model describes some of the reaction data, it does not adequately capture the effects of pH and the buffer solutions on the activity (**Fig. S8**), indicating a lack of mechanistic understanding of these effects. Therefore, future experimental kinetic studies with controlled ionic strength and benign supporting electrolytes are needed, as well as studies testing the kinetic isotope effect of H. In addition, in-situ spectroscopy to detect surface intermediates and computational simulations that include the influence of pH are necessary to understand this reaction better. Particularly, electrochemical-specific considerations need to be addressed to accurately model the effect of pH for ENO₃RR, as the effect of pH is different from what is observed for TNO₃RR.

Economic Evaluation of TNO₃RR and ENO₃RR for Ammonia Production

We evaluate the costs of electricity for ENO₃RR catalysts and hydrogen costs for TNO₃RR catalysts to produce NH₄NO₃ and the rate of NH₃ production as a simple metric to compare different catalyst under multiple operating conditions (**Fig. 5**). Successful implementation of this technology could provide over 34 million tonnes of NH₃ from nitrate conversion.[15] The ideal catalytic system must have lower NH₄NO₃ costs than the USDA standard to be feasibly implemented and maintain similar or higher NH₃ production rates than the current Haber-Bosch processes (0.2 mol g⁻¹ hr⁻¹).[72,73] In our analysis, PtRu/C in pH 1 and 7 solutions for ENO₃RR have electricity costs at or lower than USDA standards for NH₄NO₃.[74] There would be an additional cost of maintaining the pH at the desired level that is not incorporated in this model. See the SI for the balanced reactions and overall change in pH for the system. However, the

NH$_3$ production rates are 1 to 2 orders of magnitude lower than needed to meet the current industrial NH$_3$ synthesis process in our limited scope of using carbon felts in a batch reactor system, which is lower than the RDE values (more discussion in the SI). Further analysis in a flow reactor that removes mass transfer limitations should be used to assess more accurate ammonia production rates. For comparison, we also evaluate the $/tonne of NH$_4NO_3$ production for a strained Ru catalyst, which was reported to have among the highest electrochemical NH$_3$ production rates.[12] Strained Ru also achieves nearly 100% FE toward NH$_3$ at −0.2 V vs. RHE at basic conditions, which results in lower electricity cost per tonne of NH$_4$NO$_3$ than the current USDA standard price.

The hydrogen cost and rate of NH$_3$ production is also provided for PtRu/C for TNO$_3$RR in pH 1 and 7. In this reaction system, the primary cost for the production of NH$_4$NO$_3$ is H$_2$, which ranges from $2.50/kg to $6.80/kg based on electrolysis of water in proton exchange membrane cells assuming electricity costs to be $0.07/kWh.[75,76] Assuming all unused H$_2$ in the reactor will be recycled, the H$_2$ cost per tonne of NH$_4$NO$_3$ at both pH values is the same. Depending on the regional cost of H$_2$, the cost of NH$_4$NO$_3$ varies between $252/tonne up to $685/tonne. However, the rate of NH$_3$ production for PtRu/C at pH 1 is three times higher than the rate at pH 7 and two times higher than the current NH$_3$ rates from the Haber-Bosch process, making TNO$_3$RR in acidic conditions on PtRu/C a sustainable alternative process. We note that electricity and hydrogen costs are only a
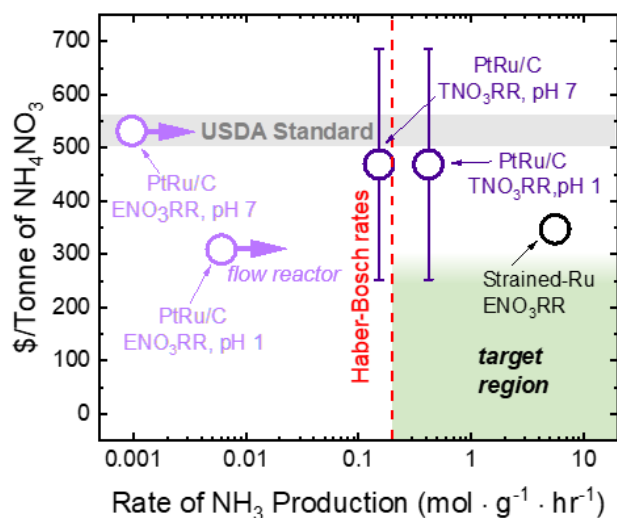

Fig. 5 Comparative electricity (ENO$_3$RR) and H$_2$ (TNO$_3$RR) cost per tonne of NH$_4$NO$_3$ vs. the rate of NH$_3$ production for TNO$_3$RR and ENO$_3$RR PtRu/C at pH 1 and 7 per gram of metal. For TNO$_3$RR (dark purple), the cost of H$_2$ was ranged from $2.50/kg to $6.80 /kg (error bars), which is the current standard for H$_2$ production from PEM cells with $0.07/kWh.[71,72] For ENO$_3$RR, the electricity cost was assumed to be $0.07/kWh with experimentally measured FE towards ammonia (93% for pH 1 and 54% for pH 7) and a total cell voltage of 1.53 V. The large light purple arrows indicate potential increase in ammonia production rates in flow system without mass transfer limitations. The value for the strained Ru catalyst for ENO$_3$RR is from Ref. [12] and corresponds to a FE of 99% and total cell voltage of 1.83 V. The gray area represents the USDA standard cost per tonne of NH$_4$NO$_3$,[70] and the dashed red line represents the current NH$_3$ production rate from the industrial Haber-Bosch process with Ru catalysts. The green block indicates the range for an ideal catalyst based on cost factors and production capabilities.

portion of the total operating costs of this process, and a full detailed technoeconomic study would be needed to accurately identify the cost of this process. However, the economic analysis presented here can be used as an initial benchmark to evaluate promising catalysts and target improvements for implementation of sustainable ammonia in place of the Haber-Bosch process.

Conclusions

This study presents a series of kinetic comparisons between thermocatalytic and electrocatalytic nitrate reduction by Pt/C, PtRu/C, and Pt$_{75}$Ru$_{25}$/C that reveals details in the mechanisms for both reactions. These findings are valuable to understand the mechanism of nitrate reduction and highlight the utility of comparing thermocatalytic and electrocatalytic reactions to clarify catalytic mechanisms. We identify similarities between the TNO$_3$RR and ENO$_3$RR showing that the hydrogen driving force and nitrate concentration increases the reaction activity. We show that changing the alloy composition of Pt$_x$Ru$_y$/C lead to similar activity trends for both TNO$_3$RR and ENO$_3$RR. This finding shows that catalysts can be screened by considering the material properties that result in high activity for both TNO$_3$RR and ENO$_3$RR, namely nitrate and hydrogen adsorption strength, supporting the use of volcano plots for these reactions. However, we also identify major differences between the two reactions such as the apparent activation energy and effect of pH on activity, indicating that there are reaction effects and changes to the mechanism related to electrochemical processes that are unique to ENO$_3$RR. This finding is consistent with the growing body of literature emphasizing the importance of considering pH for electrocatalytic reactions. To isolate pH effects and further elucidate the nitrate reduction mechanism, additional ENO$_3$RR tests that account for the ionic strength and point of zero free charge of the buffer solution and product quantification at different pH values are needed. The study here highlights the value in comparing thermocatalytic and electrocatalytic reactions for the same catalysts for both mechanistic insight and identifying the practicality of implementation.

Author Contributions

Zixuan Wang: Experimental methodology, formal data collection and analysis, writing − original draft, review, editing. Evan M. Ortiz: formal data collection and analysis, writing − review, editing. Bryan R. Goldsmith: supervision, writing − review, editing. Nirala Singh: supervision, writing − review, editing.

Conflicts of interest

There are no conflicts to declare.

Acknowledgements

References

1   M. J. Pennino, J. E. Compton and S. G. Leibowitz, *Environ Sci Technol*, 2017, **51**, 13450–13460.

2   1981, 531.

3   M. H. Ward, R. R. Jones, J. D. Brender, T. M. de Kok, P. J. Weyer, B. T. Nolan, C. M. Villanueva and S. G. van Breda, *Int J Environ Res Public Health*.

4   *National Academy of Engineering Grand Challenges For Engineers*, National Academy of Engineering, 2017.

5   C. J. Werth, C. Yan and J. P. Troutman, *ACS EST Eng.*, 2021, **1**, 6–20.

6   F. Rezvani, M.-H. Sarrafzadeh, S. Ebrahimi and H.-M. Oh, *Environ Sci Pollut Res Int*, 2019, **26**, 1124–1141.

7   N. Singh and B. R. Goldsmith, *ACS Catal.*, 2020, **10**, 3365–3371.

8   Z. Wang, D. Richards and N. Singh, *Catal. Sci. Technol.*, 2021, **11**, 705–725.

9   P. H. van Langevelde, I. Katsounaros and M. T. M. Koper, *Joule*, 2021, **5**, 290–294.

10 N. Barrabés and J. Sá, *Appl Catal B*, 2011, **104**, 1–5.

11 G. Tokazhanov, E. Ramazanova, S. Hamid, S. Bae and W. Lee, *Chem. Eng. J.*, 2020, **384**, 123252.

12 J. Li, G. Zhan, J. Yang, F. Quan, C. Mao, Y. Liu, B. Wang, F. Lei, L. Li, A. W. M. Chan, L. Xu, Y. Shi, Y. Du, W. Hao, P. K. Wong, J. Wang, S.-X. Dou, L. Zhang and J. C. Yu, *J. Am. Chem. Soc.*, 2020, **142**, 7036–7046.

13 J. M. McEnaney, S. J. Blair, A. C. Nielander, J. A. Schwalbe, D. M. Koshy, M. Cargnello and T. F. Jaramillo, *ACS Sustainable Chem. Eng.*, 2020, **8**, 2672–2681.

14 Y. Wang, A. Xu, Z. Wang, L. Huang, J. Li, F. Li, J. Wicks, M. Luo, D.-H. Nam, C.-S. Tan, Y. Ding, J. Wu, Y. Lum, C.-T. Dinh, D. Sinton, G. Zheng and E. H. Sargent, *J. Am. Chem. Soc.*, 2020, **142**, 5702–5708.

15 W. A. Tarpeh and X. Chen, *Environ. Sci. Ecotechnol.*, 2021, **5**, 100078.

16 J. Nørskov, J. Chen, R. Miranda, T. Fitzsimmons and R. Stack, *Sustainable Ammonia Synthesis–Exploring the scientific challenges associated with discovering alternative, sustainable processes for ammonia production*, US DOE Office of Science, 2016.

17 S. Jung, S. Bae and W. Lee, *Environ. Sci. Technol.*, 2014, **48**, 9651–9658.

18 Q. Wang, W. Wang, B. Yan, W. Shi, F. Cui and C. Wang, *Chem. Eng. J.*, 2017, **326**, 182–191.

19 T. Ye, D. P. Durkin, N. A. Banek, M. J. Wagner and D. Shuai, *ACS Appl. Mater. Interfaces*, 2017, **9**, 27421–27426.

20 W. Sun, W. Yang, S. Gao, Z. Xu, Q. Du, L. Chen and Q. Li, *Chem. Eng. J.*, 2020, **390**, 124617.

21 J. Martínez, A. Ortiz and I. Ortiz, *Appl. Catal., B*, 2017, **207**, 42–59.

22 M. Duca and M. T. M. Koper, *Energy Environ. Sci.*, 2012, **5**, 9726–9742.

23 G. E. Dima, A. C. A. de Vooys and M. T. M. Koper, *J. Electroanal. Chem.*, 2003, **554–555**, 15–23.

24 K. Shimazu, R. Goto and K. Tada, *Chem. Lett.*, 2002, **31**, 204–205.

25 J.-X. Liu, D. Richards, N. Singh and B. R. Goldsmith, *ACS Catal.*, 2019, **9**, 7052–7064.

26 S. Hörold, K.-D. Vorlop, T. Tacke and M. Sell, *Catal. Today*, 1993, **17**, 21–30.

27 K.-D. Vorlop and T. Tacke, *Chemie Ingenieur Technik*, 1989, **61**, 836–837.

28 Y. Song, O. Y. Gutiérrez, J. Herranz and J. A. Lercher, *Appl. Catal., B*, 2016, **182**, 236–246.

29 Y. Song, U. Sanyal, D. Pangotra, J. D. Holladay, D. M. Camaioni, O. Y. Gutiérrez and J. A. Lercher, *J. Catal.*, 2018, **359**, 68–75.

30 R. Bababrik, D. Santhanaraj, D. E. Resasco and B. Wang, *J Appl Electrochem*, 2021, **51**, 19–26.

31 J. S. Adams, M. L. Kromer, J. Rodríguez-López and D. W. Flaherty, *J. Am. Chem. Soc.*, 2021, **143**, 7940–7957.

32 D. Koshy, S. Nathan, A. Asundi, A. Abdellah, S. Dull, D. Cullen, D. Higgins, Z. Bao, S. Bent and T. Jaramillo, *Angew. Chem. Int. Ed.*, , DOI:https://doi.org/10.1002/anie.202101326.

33 Z. Wang, S. D. Young, B. R. Goldsmith and N. Singh, *J. Catal.*, 2021, **395**, 143–154.

34 O. A. Baturina, S. R. Aubuchon and K. J. Wynne, *Chem. Mater.*, 2006, **18**, 1498–1504.

35 O. A. Pinchuk, S. R. Aubuchon, C. Marks, R. Dominey, F. Dundar, O. F. Deniz, A. Ata and K. J. Wynne, *Fuel Cells*, 2009, **9**, 554–561.

36 J. Zheng, W. Sheng, Z. Zhuang, B. Xu and Y. Yan, *Science Advances*, 2016, **2**, e1501602.

37 P. Singh, M. K. Singh, Y. R. Beg and G. R. Nishad, *Talanta*, 2019, **191**, 364–381.

38 P. Kurniawati, R. Gusrianti, B. B. Dwisiwi, T. E. Purbaningtias and B. Wiyantoko, *AIP Conference Proceedings*, 2017, **1911**, 020012.

39 D. Zhu, L. Zhang, R. E. Ruther and R. J. Hamers, *Nat. Mater.*, 2013, **12**, 836–841.

40 N. Singh, Y. Song, O. Y. Gutiérrez, D. M. Camaioni, C. T. Campbell and J. A. Lercher, *ACS Catal.*, 2016, **6**, 7466–7470.

41 J. Ryu, D. T. Bregante, W. C. Howland, R. P. Bisbey, C. J. Kaminsky and Y. Surendranath, *Nat Catal*, 2021, 1–11.

42 Z. J. Schiffer, A. M. Limaye and K. Manthiram, *Joule*, 2021, **5**, 135–148.

43 F. Epron, F. Gauthard, C. Pinéda and J. Barbier, *J. Catal.*, 2001, **198**, 309–318.

44 J. Hirayama, K. Yasuda, S. Misu, R. Otomo and Y. Kamiya, *Catal. Sci. Technol.*, 2019, **9**, 4017–4022.

45 I. Mikami, Y. Sakamoto, Y. Yoshinaga and T. Okuhara, *Appl. Catal., B*, 2003, **44**, 79–86.

46 M. T. de Groot and M. T. M. Koper, *J. Electroanal. Chem.*, 2004, **562**, 81–94.

47 J. Yang, Y. Kwon, M. Duca and M. T. M. Koper, *Anal. Chem.*, 2013, **85**, 7645–7649.

48 S. D. Ebbesen, B. L. Mojet and L. Lefferts, *J. Phys. Chem. C*, 2011, **115**, 1186–1194.

49 A. Pintar, J. Batista, J. Levec and T. Kajiuchi, *Appl. Catal., B*, 1996, **11**, 81–98.

50 I. Witońska, S. Karski and J. Gołuchowska, *Kinet Catal*, 2007, **48**, 823–828.

51 I. Povar and O. Spinu, *J. Electrochem. Sci. Eng.*, 2016, **6**, 145–153.

52 J. Yang, P. Sebastian, M. Duca, T. Hoogenboom and M. T. M. Koper, *Chem. Commun.*, 2014, **50**, 2148–2151.

53 G. Horányi and E. M. Rizmayer, *J. Electroanal. Chem. Interfacial Electrochem.*, 1982, **140**, 347–366.

54 G. Horányi and M. Wasberg, *Electrochim. Acta*, 1997, **42**, 261–265.

55 M. Wasberg and G. Horányi, *Electrochim. Acta*, 1995, **40**, 615–623.

56 X. Qin, L. Zhang, G.-L. Xu, S. Zhu, Q. Wang, M. Gu, X. Zhang, C. Sun, P. B. Balbuena, K. Amine and M. Shao, *ACS Catal.*, 2019, **9**, 9614–9621.

57 N. Singh, M.-S. Lee, S. A. Akhade, G. Cheng, D. M. Camaioni, O. Y. Gutiérrez, V.-A. Glezakou, R. Rousseau, J. A. Lercher and C. T. Campbell, *ACS Catal.*, 2019, **9**, 1120–1128.

58 A. D. Wiesner, L. E. Katz and C.-C. Chen, *J. Colloid Interface Sci.*, 2006, **301**, 329–332.

59 G. Jerkiewicz, *ACS Catal.*, 2020, **10**, 8409–8417.

60 F. Silva, M. J. Sottomayor and A. Hamelin, *J. Electroanal. Chem. Interfacial Electrochem.*, 1990, **294**, 239–251.

61 R. Rizo, E. Sitta, E. Herrero, V. Climent and J. M. Feliu, *Electrochim. Acta*, 2015, **162**, 138–145.

62 A. Ganassin, P. Sebastián, V. Climent, W. Schuhmann, A. S. Bandarenka and J. Feliu, *Sci. Rep.*, 2017, **7**, 1246.

63 N. García-Aráez, V. Climent and J. M. Feliu, *J. Am. Chem. Soc.*, 2008, **130**, 3824–3833.

64 I. Ledezma-Yanez, W. D. Z. Wallace, P. Sebastián-Pascual, V. Climent, J. M. Feliu and M. T. M. Koper, *Nat. Energy*, 2017, **2**, 1–7.

65 F. J. Sarabia, P. Sebastián-Pascual, M. T. M. Koper, V. Climent and J. M. Feliu, *ACS Appl. Mater. Interfaces*, 2019, **11**, 613–623.

66 J. Zheng, Z. Zhuang, B. Xu and Y. Yan, *ACS Catal.*, 2015, **5**, 4449–4455.

67 I. T. McCrum and M. J. Janik, *J. Phys. Chem. C*, 2016, **120**, 457–471.

68 J. Zheng, J. Nash, B. Xu and Y. Yan, *J. Electrochem. Soc.*, 2018, **165**, H27.

69 T. Cheng, L. Wang, B. V. Merinov and W. A. Goddard, *J. Am. Chem. Soc.*, 2018, **140**, 7787–7790.

70 L. Rebollar, S. Intikhab, N. J. Oliveira, Y. Yan, B. Xu, I. T. McCrum, J. D. Snyder and M. H. Tang, *ACS Catal.*, 2020, **10**, 14747–14762.

71 V. Briega-Martos, E. Herrero and J. M. Feliu, *Electrochim. Acta*, 2017, **241**, 497–509.

72 F. Haber and R. L. Rossignol, *Zeitschrift für Elektrochemie und angewandte physikalische Chemie*, 1913, **19**, 53–72.

73 T. Kandemir, M. E. Schuster, A. Senyshyn, M. Behrens and R. Schlögl, *Angew. Chem. Int. Ed.*, 2013, **52**, 12723–12726.

74 USDA ERS - Fertilizer Use and Price, https://www.ers.usda.gov/data-products/fertilizer-use-and-price.aspx, (accessed July 20, 2020).

75 A. T. Mayyas, M. F. Ruth, B. S. Pivovar, G. Bender and K. B. Wipke, *Manufacturing Cost Analysis for Proton Exchange Membrane Water Electrolyzers*, 2019.

76 J. Vickers, D. Peterson and K. Randolph, *Cost of Electrolytic Hydrogen Production with Existing Technology*, Department of Energy, 2021.